Supporting Information

Liquid–free ionic conductive elastomers with high mechanical properties and ionic conductivity for multifunctional sensors and triboelectric nanogenerators

Fangyan Ou, Ting Xie, Xinze Li, Zhichao Zhang, Chuang Ning, Liang Tuo, Wenyu Pan, Changsheng Wang, Xueying Duan, Qihua Liang, Wei Gao, Zequan Li,* and Shuangliang Zhao

1. Experimental Section

1.1. Materials

Polytetramethylene ether glycol (PTMEG, M_n = 2000 g·mol^{-1}), 4,4'–dicyclohexylmethane diisocyanate (HMDI, >90.0%), 4,4–Diphenylmethane bismaleimide (BMI, >96.0%), Dibutyltin dilaurate (DBTDL, 95%), and 3,3'–Dithiopropionic acid dimethylester (>96.0%) were purchased from Shanghai Aladdin Biochemical Technology Co., Ltd. 2,5–Furandimethanol (BHMF, 98%), N, N–Dimethylacetamide (DMAC, 99.8%), Bis(trifluoromethane)sulfonimide lithium salt (LiTFSI, 98.0%) were purchased from Anhui Senrise Technology Co., Ltd. Diamine hydrate (>80.0%), Methanol (analytically pure, AR) were purchased from Nanning Blue Sky Experimental Equipment Co., Ltd. Polymethylmethacrylate (PMMA) films, polyethylene terephthalate (PET) films, polydimethylsiloxane (PDMS) films and polytetrafluoroethylene (PTFE) films were all purchased from commercially available. All reagents were used as the original without further purification.

1.2. Preparation of 3,3'–dithiobis (propionohydrazide) (DPH)

DPH was synthesized according to the methods provided in the literature as shown in Fig. S1[1] 3,3' –Dithiopropionic acid dimethylester (1.19 g, 4.2 mmol) was dissolved in methanol (25.0 ml). Diamine hydrate (1.24 ml, 2.5 mmol) was added dropwise, and the reaction was stirred overnight at room temperature. After the reaction, the reaction solution was filtered to separate some solid products, and the product was washed with methanol (30.0 ml) two times. Finally, the obtained product was dried at 60 °C for 24 h. The purity of the DPH was characterized by ^{1}H–NMR (600 MHz, DMSO–d$_6$, 25 °C, TMS):1δ 9.06 (s, 2H), 4.19 (d, J = 4.1 Hz, 4H), 2.89 (t, J = 7.2 Hz, 4H), 2.40 (t, J = 7.2 Hz, 4H).

1.3. Synthesis of double dynamic crosslinked polyurethane elastomer (SS$_x$DA$_y$)

The synthesis routes for SS$_x$DA$_y$ elastomers are shown in Fig. S2, and the specific process is as follows. First, the PTMEG (M_n = 2000 g.mol^{-1}, 5.0 g, 2.5 mmol) was added into a three–neck flask equipped with a continuous mechanical agitator, heated and stirred at 110 °C for 40 min in a vacuum environment to fully remove the moisture.

After the reaction system was cooled to 80 °C, HMDI (1.31 g, 5 mmol) was diluted with DMAc solvent (10 ml) and added to the flask, and 5 mg of DBTDL was added as a catalyst. The reaction system was further heated at 80 °C under N_2 environment stirring for 4 h to generate –NCO capped polyurethane prepolymer. The ratio of physical to dynamic covalent cross–linked was modulated by changing the ratio of DPH and BHMF. As an example, $SS_{50}DA_{50}$ was prepared by adding appropriate amounts of DPH (0.298 g, 1.25 mmol) and DMAc (30.0 ml) to the prepolymer and stirring at 40 °C for 9 h. BHMF (0.16 g, 1.25 mmol) and DMAc (15.0 ml) were then added and reacted at 80 °C for 8 h. Finally, BMI (0.336 g, 0.625 mmol) was added as a cross–linked agent and stirred for 4 h. Upon completion of the reaction, the yellowish and transparent viscous solution was obtained, which was poured into a glass petri dish and placed on a hot plate at 80 °C for heating and slow evaporation of the solvent, and then dried under vacuum at 80 °C for 48 h to obtain a polyurethane elastomer with a double cross–linked network. Similarly, SS_{100} (DPH, 0.595 g, 2.5 mmol), $SS_{75}DA_{25}$ (DPH, 0.446 g, 1.875 mmol; BHMF, 0.08 g, 0.625 mmol; BMI, 0.168 g, 0.3125 mmol), $SS_{25}DA_{75}$ (DPH, 0.146 g, 0.625 mmol; BHMF, 0.24 g, 1.875 mmol; BMI, 0.504 g, 0.9375 mmol), DA_{100} (BHMF, 0.32 g, 2,5 mmol; BMI 0.673 g, 1.25 mmol) were prepared in the same way as above.

1.4. Preparation of $SS_{50}DA_{50}$–LiTFSI$_{z\%}$ ionic conductive elastomer

The different proportions of LiTFSI (mass fraction: 20 wt.% to 100 wt.%) were completely dissolved in DMAc and mixed with the $SS_{50}DA_{50}$ solution obtained by the above reaction for 4 h. After pouring the obtained mixed solution into a glass petri dish and slowly evaporate on a hot plate at 80 °C the solvent was evaporated to obtain the $SS_{50}DA_{50}$–LiTFSI$_{z\%}$ (z represents the difference between LiTFSI and the mass percentage of polyurethane solid contents, which were 20, 40, 60, 80 and 100, respectively). After that, the samples were hot–pressed at 120 °C for 5 min to obtain a smooth and transparent film.

1.5. Fabrication of the $SS_{50}DA_{50}$–LiTFSI$_{80\%}$–based sensors and TENGs

The $SS_{50}DA_{50}$–LiTFSI$_{80\%}$ samples were cut into rectangular strips with a shape of 30 ×

6×5 mm^3, and two ends were connected with wires, respectively. For the measurement, the assembled sensors were fixed to different joints of the human body with 3M adhesive tapes. The ICE–TENG was fabricated by using an acrylic plate (4×4 cm^2) as the substrate, SS$_{50}$DA$_{50}$–LiTFSI$_{80\%}$ film as the positive triboelectric layer material, and PE, PET, PDMS, and PTFE films as the negative triboelectric layer material. Steel and silver wires were used to connect the electrodes to the external loads for the test.

1.6. Materials characterization

1.6.1. General characterization

The ^{1}H NMR (600 MHz) spectra were measured on a 600 MHz NMR spectrometer (Bruker AVANCE III). The infrared spectra were obtained by Fourier infrared spectrometer (ATR–FTIR, IRTracer–100) with a measurement range from 4000 to 650 cm^{-1}. The variable–temperature infrared spectra were measured by Nicolet iS50 equipped with a thermo controller and the measurement range was from 4000 to 400 cm^{-1}. Raman spectra (inVia Reflex) were recorded on a microscope using a laser excitation wavelength of 532 nm with a measurement range of 2000–100 cm^{-1}. The transmittance of the film was taken by UV–Vis spectrophotometer (Uv–670) with a measurement wavelength of 800–200 nm. X–ray diffraction patterns were recorded on an X–ray diffractometer (Rigaku D/MAX 2500V) with a scanning speed of 10°·min^{-1}. The small–angle X–ray scattering (SAXS) patterns were measured using the Xeuss system (Xenocs 3.0, France). The microphase structure of the samples was probed by atomic force microscopy (AFM) (Dimension Icon). Thermogravimetric analyses were performed on a differential thermogravimetric analyzer (DTA–60H) in the temperature range of 30–800 °C, and the heating rate of 10 °C·min^{-1} under N$_2$ atmosphere. Differential scanning calorimeter (DSC) experiments were performed under N$_2$ atmosphere as obtained by DSC 214 polyma test with a scanning range of -70 °C to 200 °C, and the heating rate was 10 °C·min^{-1}. Dynamic mechanical analyses (DMA) were performed on the Dynamic Mechanical Analyzer (DMA850) in tension mode in the temperature range from -100 to 150 °C with a heating rate of 10 °C·min^{-1}. Optical microscope images were taken by a polarized light microscope (POM)

(LAS4.6.0/DM6000B–M) equipped with a thermal controller.

1.6.2. Mechanical properties tests

The mechanical experiments were performed at room temperature by BZ2.5/pN1S material mechanical test system (ZWICK, Germany).

(1) The samples were prepared as a dumbbell–shaped strips (effective area: 14.0 mm × 2.0 mm × 0.7 mm). All the tensile speeds were set to 50 mm·min^{-1}, and at least five individual tensile tests were performed for each sample. The tensile stress (σ) and elongation at break (ε) are calculated from the stress–strain curves, by the following equation:

$$\sigma = \frac{F}{b*d} \tag{S1}$$

$$\varepsilon = \frac{L_{\max}-L_0}{L_0} * 100\% \tag{S2}$$

where σ is the tensile stress, F is the maximum tensile force of the sample at break, b is the width of the effective area of the sample, d is the thickness of the sample, ε is the elongation at break of the sample, $L_{\max}$ is the maximum length of the sample at break, and L_0 is the standard length of the sample of 14 mm.

(2) The toughness (τ) of the sample can be obtained by calculating the area surrounded by the stress (σ)–strain (ε) curves, using the equation:

$$\tau = \int_0^{\varepsilon_{\max}} \sigma \, d\varepsilon \tag{S3}$$

where ε is the strain of the sample, σ is the stress of the sample and $\varepsilon_{\max}$ is the elongation at break of the sample.

(3) In the cyclic test experiment, the loaded/unloaded rate was measured at a constant strain rate of 50 mm·min^{-1} at room temperature. The samples were stretched to 500% strain and then loaded/unloaded five times continuously without rest. In addition, the samples were loaded/unloaded at 100% strain and successively increased to 700%. The first cycle curves of SS$_{50}$DA$_{50}$ are shown below. The hysteresis loop area and hysteresis ratio were calculated using the following equations:

$$Dissipated\ energy = S_s - S_r * 100\% \tag{S4}$$

$$Hysteresis\ ratios = \frac{S_s - S_r}{S_s} * 100\% \tag{S5}$$

where S_s is the area of the boundary between the stretch curve and the X–axis, and S_r is the area of the boundary between the rebound curve and the X–axis.

(4) The fracture energy test was conducted by Greensmith's test method at a stretching rate of 3 mm·min^{-1} for notched (length of the crack is 1 mm) and unnotched samples (gauge length of 10.0 mm, width of 5.0 mm, thickness of 0.8 mm). The fracture energy (G_c) of the sample was calculated by:

$$G_c = \frac{6wc}{\sqrt{\lambda_c}} \tag{S6}$$

where λ_c represents the elongation at the break of the notched sample, c is the length of the notch of 1.0 mm, and w represents the strain energy calculated by integrating the stress–strain curve of the unnotched specimen until ε_c ($\varepsilon_c=\lambda_c-1$).

1.6.3. Healing efficiency test

The healing efficiency was evaluated by stress–strain curves. The dumbbell–shaped samples were cut, and then placed in full contact on a hot plate at 130 °C for repair. After healing, the self–healed samples were subjected to tensile tests. The healing efficiency was calculated by the following equation:

$$H = \frac{\sigma_h}{\sigma_0} * 100\% \tag{S7}$$

where σ_0 is the tensile stress of the original sample, and σ_h is the tensile stress of the self–healed sample.

1.6.4. Ionic conductivity tests

Electrochemical impedance spectroscopy (EIS) of $SS_{50}DA_{50}$–LiTFSI$_{z\%}$ was measured using an electrochemical workstation (CHI660E, Chenhua). The samples were cut into circular specimens (64π mm^2), and the samples were sandwiched between two stainless steel electrodes with a diameter of 16 mm. The measurement temperature range was from 25 to 80 °C, and the frequency range was set from 0.001 Hz to 1.0 MHz with an amplitude of 1.0 V. Ionic conductivity is calculated using the following equation:

$$\sigma = \frac{L}{R*S} \tag{S8}$$

where L is the thickness of the sample, R is the bulk resistance of the sample (obtained from EIS), and S is the contact area between the sample and steel electrodes.

1.6.5. Sensor device testing

The resistance sensors and pressure sensors were measured by a Keithley DMM7510 multimeter, and the wires of the sensor were connected to the multimeter to record the electrical signals. The output voltage was obtained using an oscilloscope (TEKTRONIX MDO3014) with a high voltage probe (TEKTRONIX P6015A), and the short–circuit current and transferred charge were obtained by testing with an electrostatic meter (Keithley 6514). A linear motor (LinMot, Bol–37 × 166/260) produced a linear motion to trigger the TENG to work. Prior to the commencement of the research, informed written consent was obtained from all participants to ensure ethical compliance. During the experiment, samples exhibiting excellent biosafety were carefully placed on the volunteers' skin to monitor a range of human activities and electrophysiological signals. It is important to note that these procedures had no adverse physical or psychological effects on the participants, both during and after the completion of the experiment.

1.6.6. Humidity test

Saturated solutions of lithium chloride, potassium carbonate, calcium chloride, sodium chloride and zinc sulfate were prepared respectively.The resistance of the strain sensors was measured by using a Keithley DMM7510 multimeter after the samples were placed in an environment with relative humidity of 11%, 40%, 50%, 75% and 90% for 24 h.

1.6.7. Dissolution tests

Petroleum ether (PE), dimethyl silicone oil, tetrahydrofuran (THF), N,N-dimethylformamide (DMF) and toluene were used to perform organic swelling tests on $SS_{50}DA_{50}$–$LiTFSI_{80\%}$. $SS_{50}DA_{50}$–$LiTFSI_{80\%}$ was cut into short strip samples and soaked in different organic solvents for 24 h at room temperature.

1.6.8. In vitro cytotoxicity assays

The cytotoxicity of the film samples in mammary epithelial cells (MCF 10A) was measured by CCK–8 assay. The samples were immersed in Dulbecco's modified eagle medium (DMEM) at 37 °C for 24 h to get the extracts. Then the cell suspension (100 μL) was seeded in 96–well plate with 5000 cells per well and incubated at 37 °C with

5% CO_2. After the cell adheres to the plate, the medium was removed and refilled with the film samples extract (100 µL) or medium as control. Cell viability was evaluated with the CCK–8 reagent at 1 h, 3 h, 6 h, 12 h, 24 h and 48 h at 450 nm according to the manufacturer's instructions.

2.Supplementary Figures and Tables
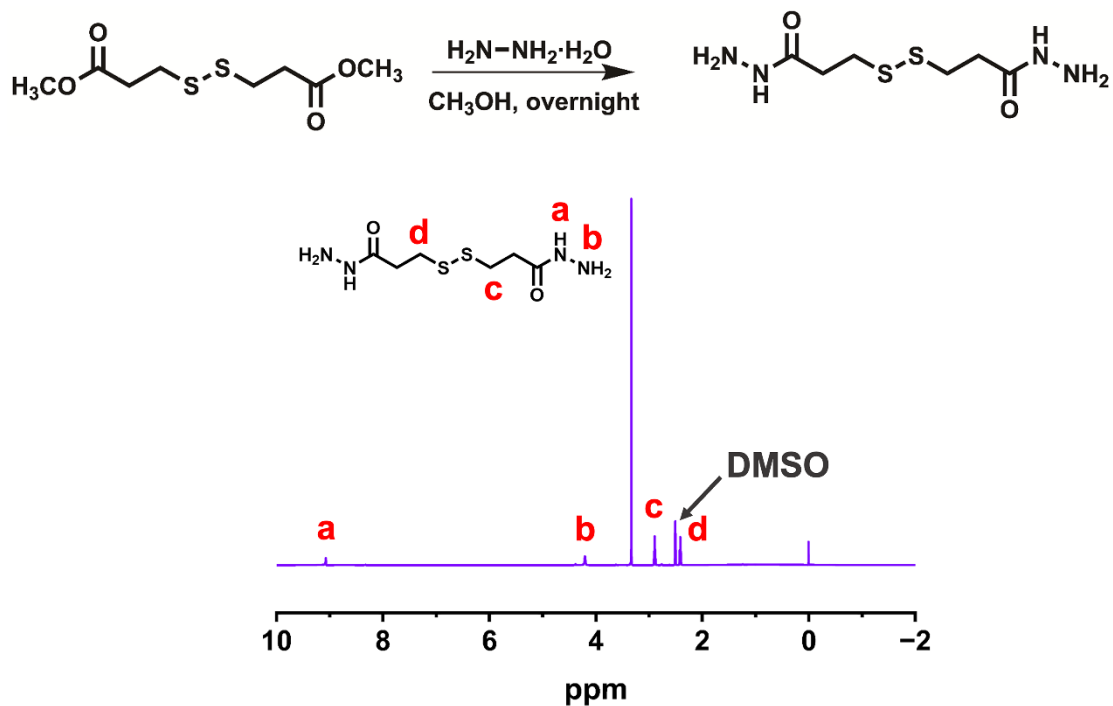
Fig. S1 Synthetic route and ^{1}H–NMR (600 MHz, DMSO–d_6) spectrum of DPH.
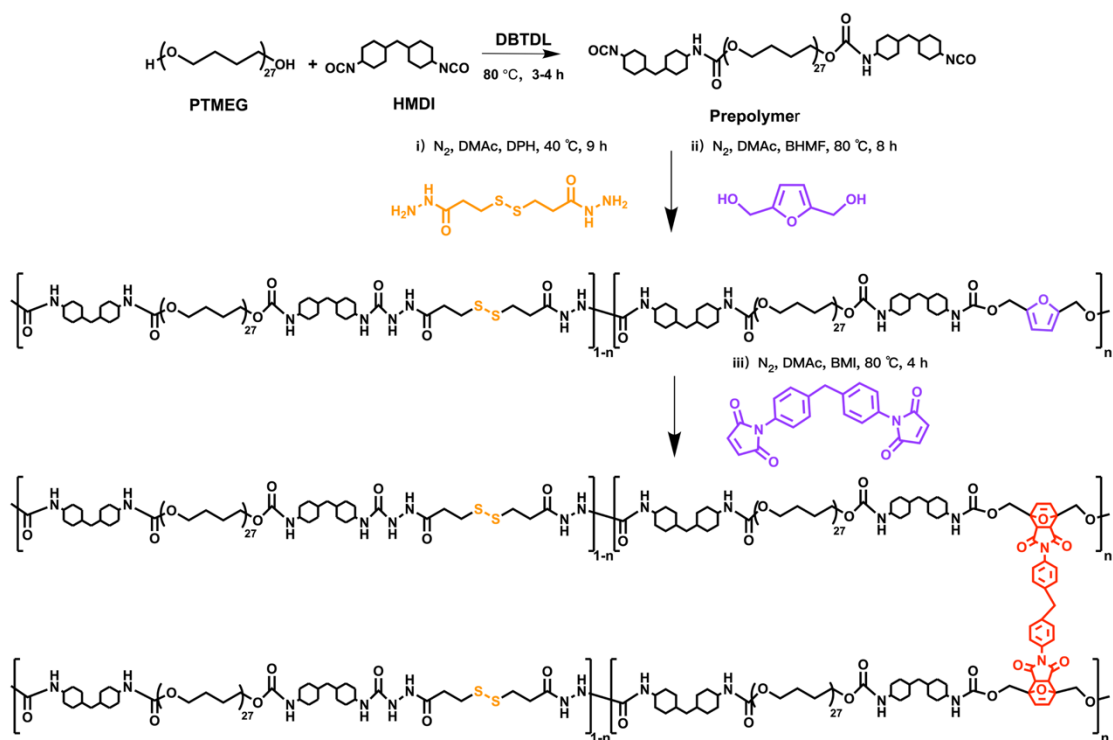
Fig. S2 Synthesis route of SS_xDA_y healing polyurethane elastomer.
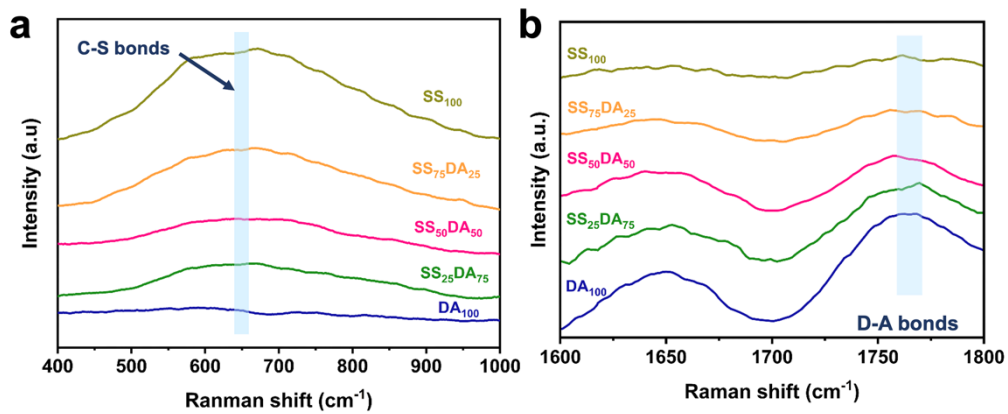
Fig. S3 Raman spectral investigation of all ratios of SS_xDA_y healing polyurethane elastomers. The peak appears at 639 cm^{-1} of the C–S bonds, and the peak occurs at 1760 cm^{-1} of the D–A bonds.
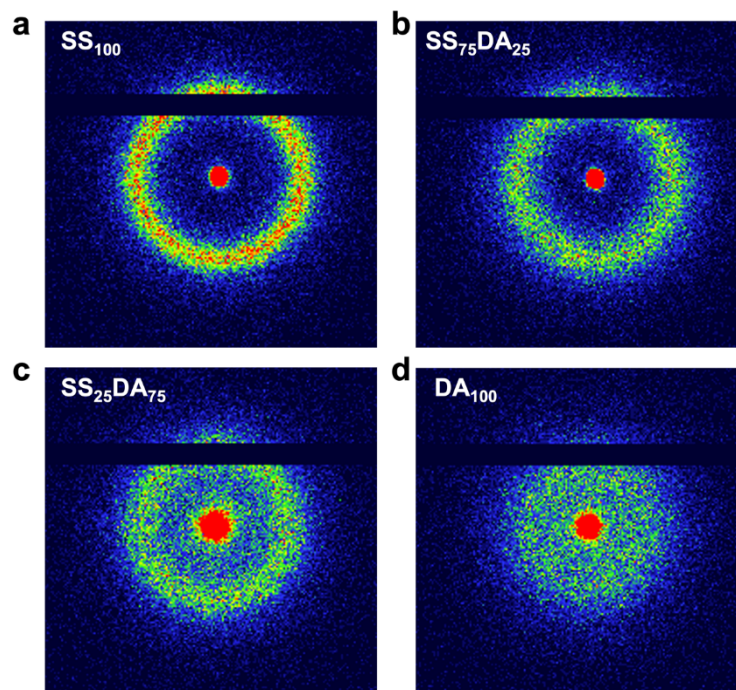
Fig. S4 2D SAXS images of SS_{100}, $SS_{75}DA_{25}$, $SS_{25}DA_{75}$ and DA_{100} samples.
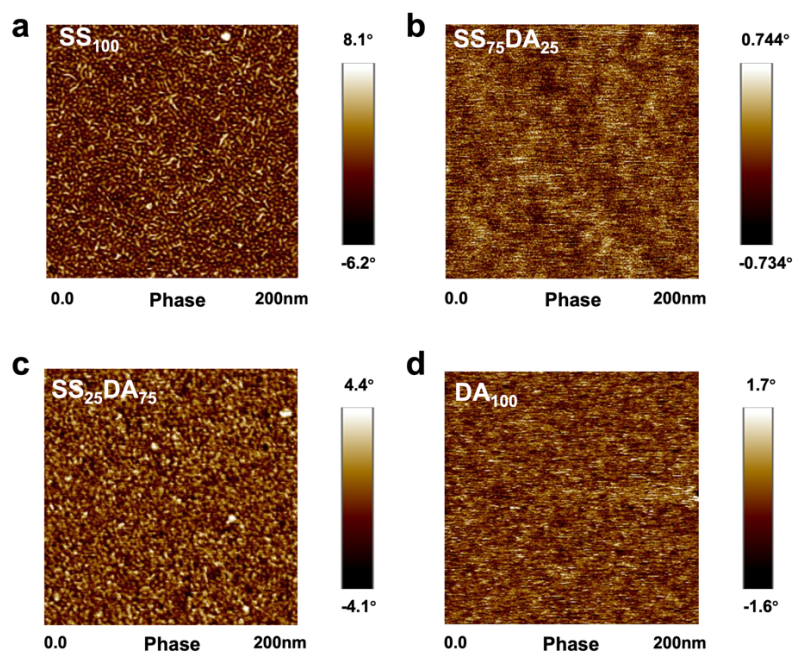
Fig. S5 AFM phase image of SS_{100}, $SS_{75}DA_{25}$, $SS_{25}DA_{75}$, and DA_{100} samples. The bright areas are hard phase and the dark areas are soft phase.
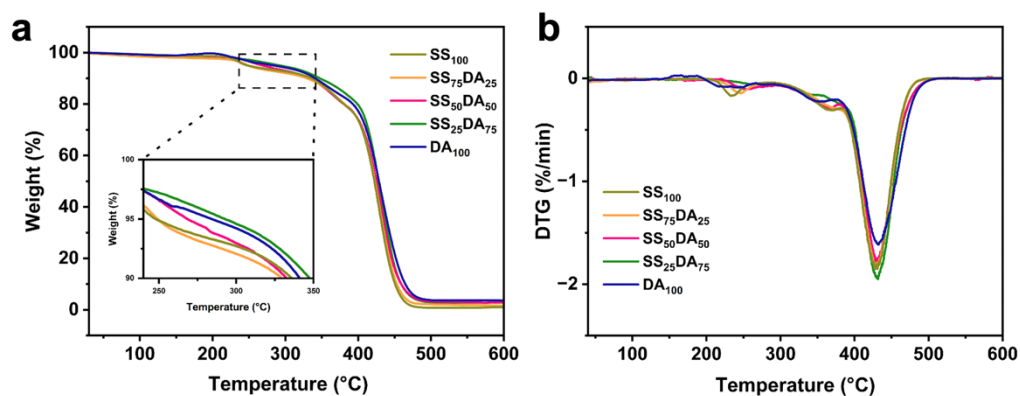
Fig. S6 TGA (a) and DTG (b) curves of all SS_xDA_y polyurethane elastomers at 10 °C·min^{-1} under N_2 atmosphere, which displays that the SS_xDA_y samples are thermally stable up to 250 °C. The DTG curves showed two weight loss peaks at 200–400 °C, one is the degradation of the imide group at about 237 °C, and the other is the degradation of the carbamate group at 350 °C.
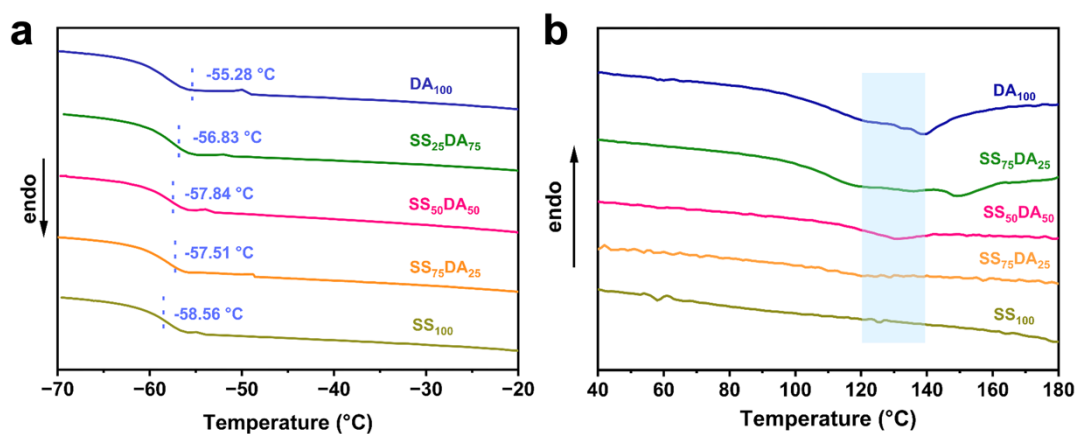
Fig. S7 DSC curves of SS$_x$DA$_y$ healing polyurethane elastomers. The results of D–A contained samples showed that there were obvious endothermic peaks near 120–140 °C, which was due to the thermally reversible reaction of D–A bonds, and the breakage of D–A bonds occurred endothermic reaction in the system.

Table S1. Mechanical experimental results of SS$_x$DA$_y$ films.

SS$_x$DA$_y$	Molar ratio (DPH: BHMF)	Stress (MPa)	Strain (%)	Toughness (MJ·m^{-3})
SS$_{100}$	100:0	29.14	1339.83	187.70
SS$_{75}$DA$_{25}$	75:25	56.34	1014.25	201.32
SS$_{50}$DA$_{50}$	50:50	58.90	1229.72	260.33
SS$_{25}$DA$_{75}$	25:75	52.91	1269.23	223.11
DA$_{100}$	0:100	7.82	869.74	34.31
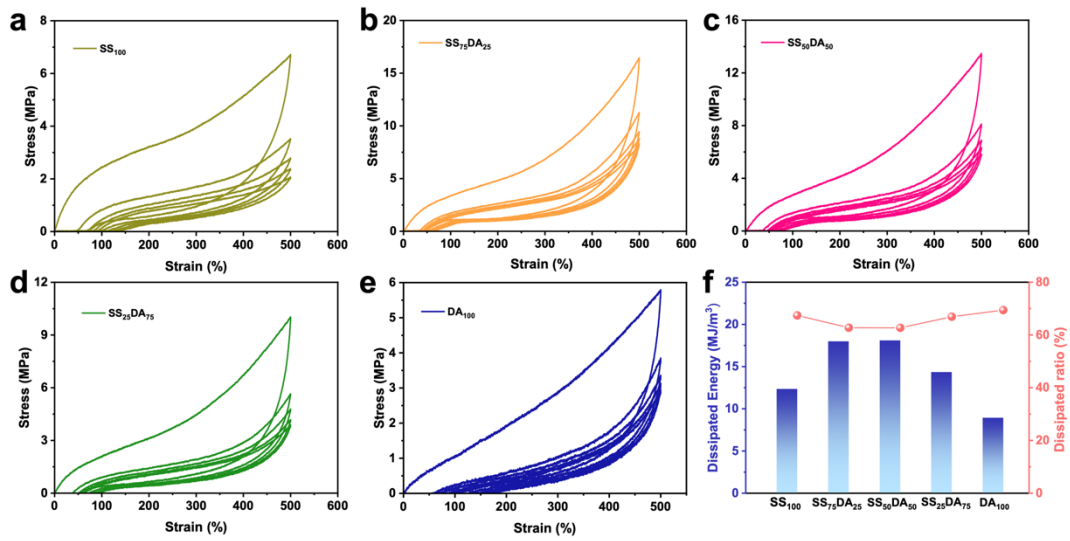
Fig. S8 a–e) Consecutive cyclic tensile curves and f) dissipation energy and hysteresis ratio required for the first cycle of SS_xDA_y polyurethane elastomers at a strain of 500%.
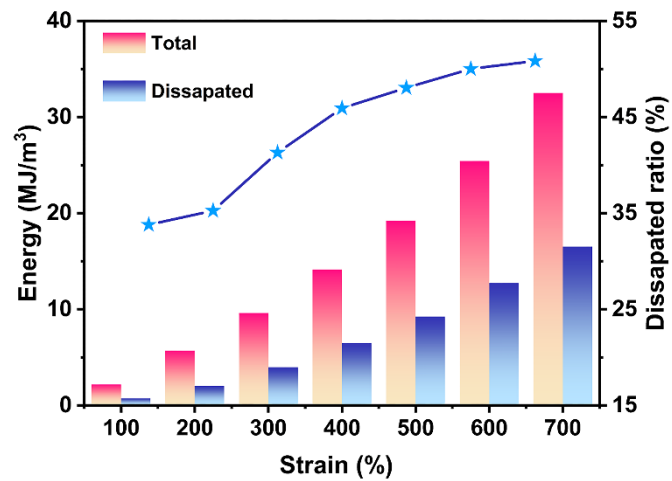
Fig. S9 Dissipated energy and hysteresis ratio for consecutive cycles with increasing strains for the $SS_{50}DA_{50}$ samples.
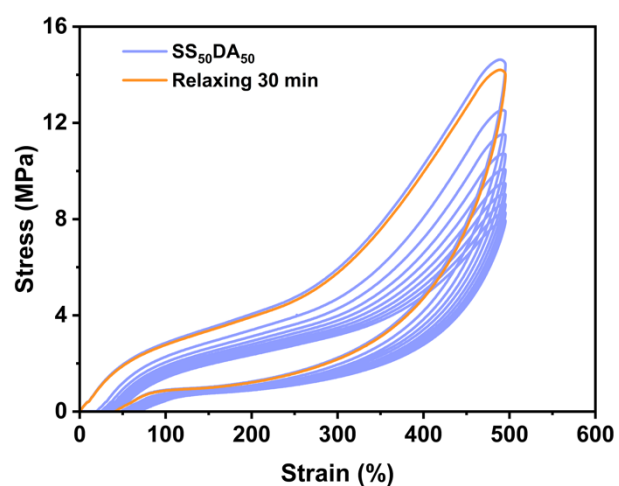
Fig. S10 Consecutive cyclic tensile curves of $SS_{50}DA_{50}$ at a strain of 500%. After relaxing for 30 min at room temperature, the cyclic curve was nearly overlapped with the first cyclic curve.
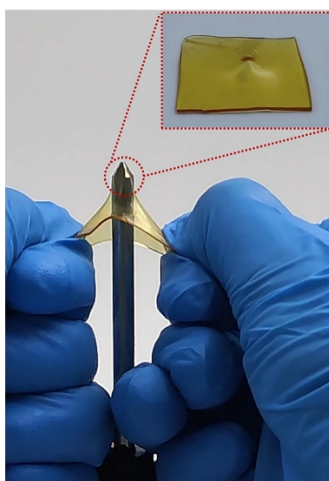
Fig. S11 Photographs showing the performance of $SS_{50}DA_{50}$ film punctured by a sharp needle, indicating the strong puncture resistance of the dual dynamically crosslinked elastomer.
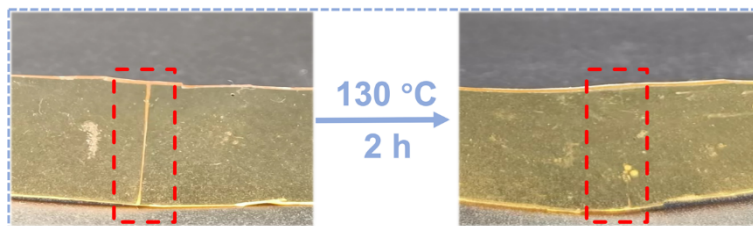
Fig. S12 Photographs of the damaged $SS_{50}DA_{50}$ film before and after healing. Healing condition: 130 °C heating for 2 h.
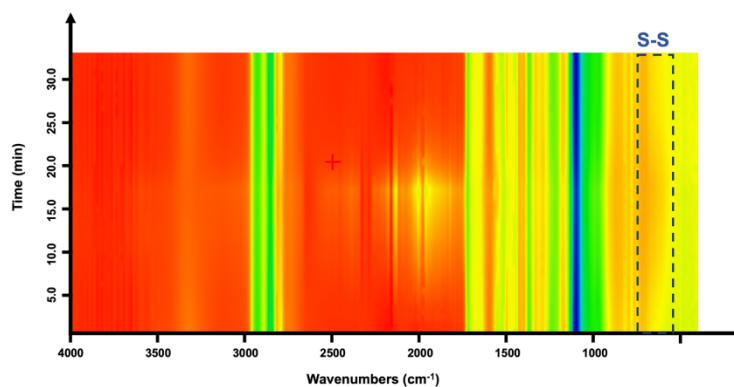
Fig. S13 Variable–temperature ATR images of $SS_{50}DA_{50}$ film during heating and cooling processes, based on 30 °C and ramping up to 130 °C.
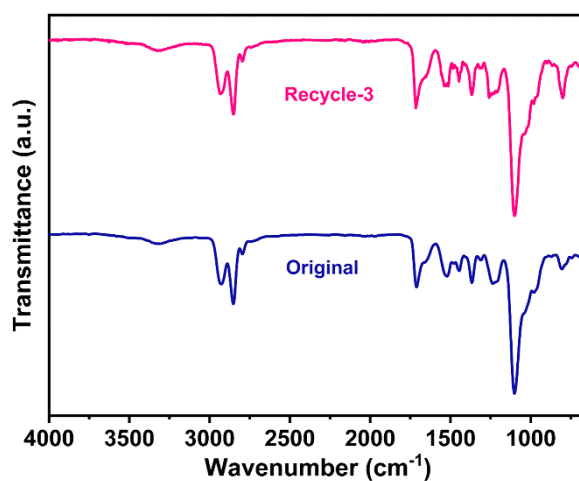
Fig. S14 FTIR spectra of pristine and solvent–assisted recycled $SS_{50}DA_{50}$ samples.
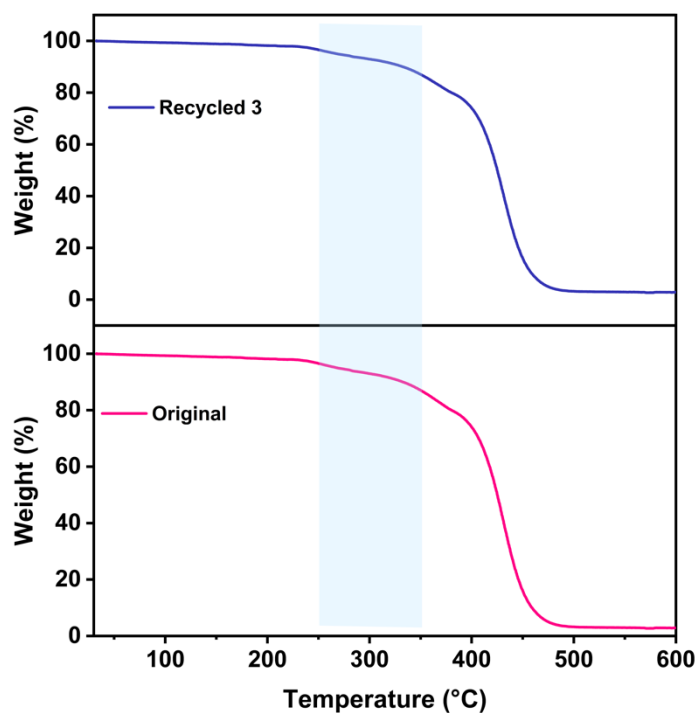
Fig. S15 The TGA curves of solvent–assisted recycled and original $SS_{50}DA_{50}$ samples.
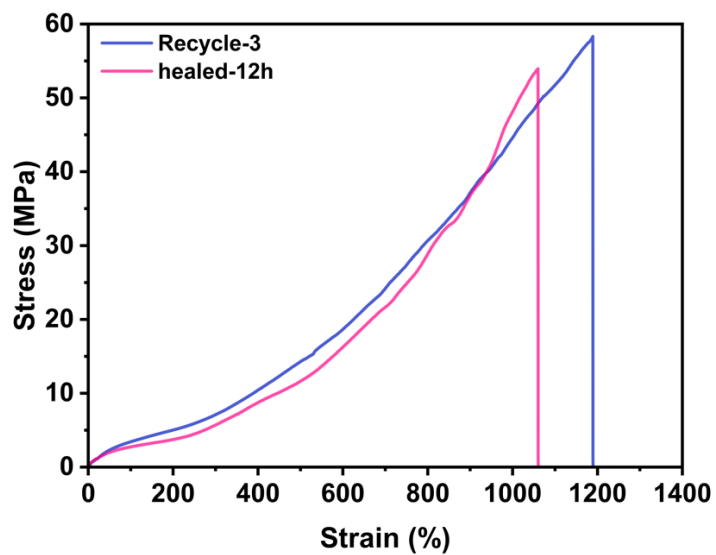
Fig. S16 The stress–strain curves of pristine and solvent–assisted recycled $SS_{50}DA_{50}$ samples.
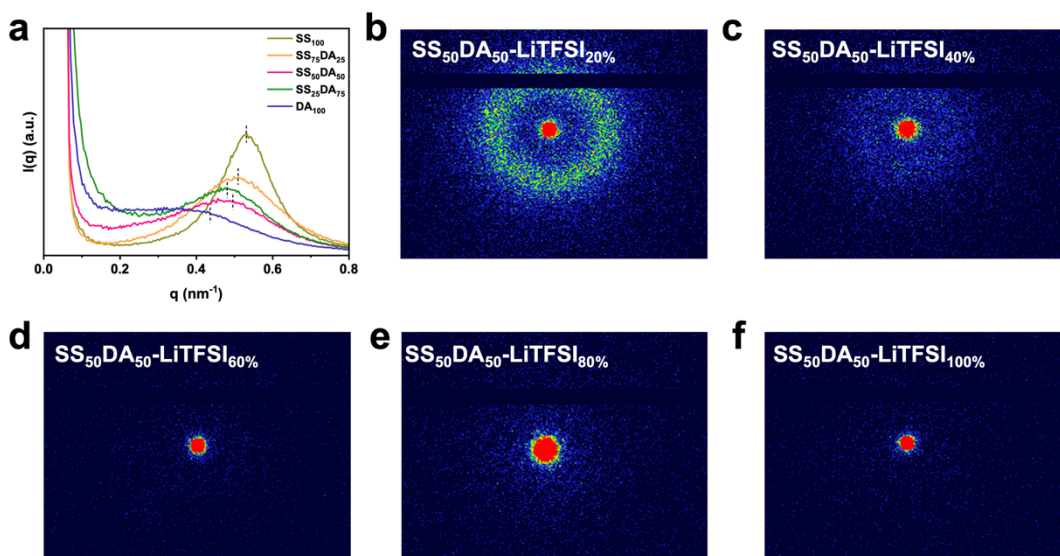
Fig. S17 a) 1D SAXS curves and b–f) 2D SAXS images of $SS_{50}DA_{50}$–LiTFSI$_{z\%}$ samples. The microphase separation structure of the samples gradually disappears with the increase of LiTFSI content, indicating that the increase of LiTFSI content hinders the accumulation of the structural domains of the hard–phase chains, which leads to the decrease of the mechanical properties.
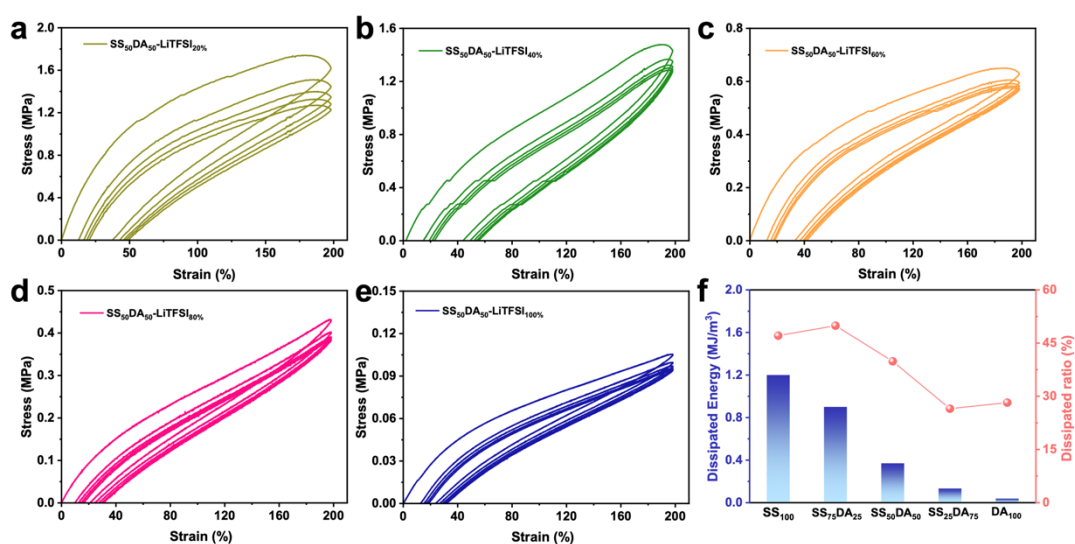
Fig. S18 a–e) Consecutive cycle tensile curves of $SS_{50}DA_{50}$–LiTFSI$_{z\%}$ ionic conductive elastomer at a strain of 500%. f) dissipation energy and hysteresis ratio required for the first cycle of $SS_{50}DA_{50}$–LiTFSI$_{z\%}$ at a strain of 500%.
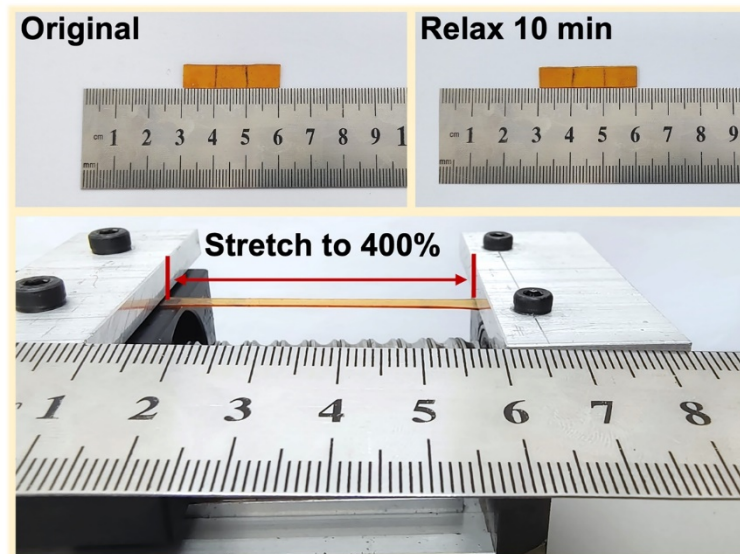
Fig. S19 Photographs of $SS_{50}DA_{50}$–$LiTFSI_{80\%}$ film that can be restored to its original length after being stretched to 400% strain.
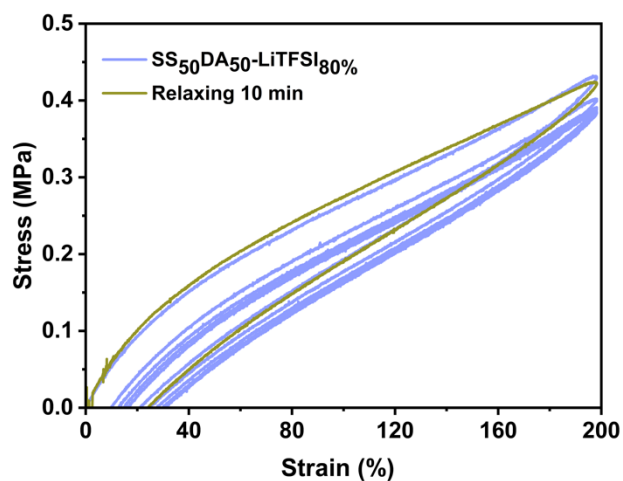
Fig. S20 Consecutive cyclic tensile curves of $SS_{50}DA_{50}$–$LiTFSI_{80\%}$ ionic conductive elastomer at 500% strain. After 10 min at room temperature, the cyclic curve was almost exactly overlapped with the first cycle curve.
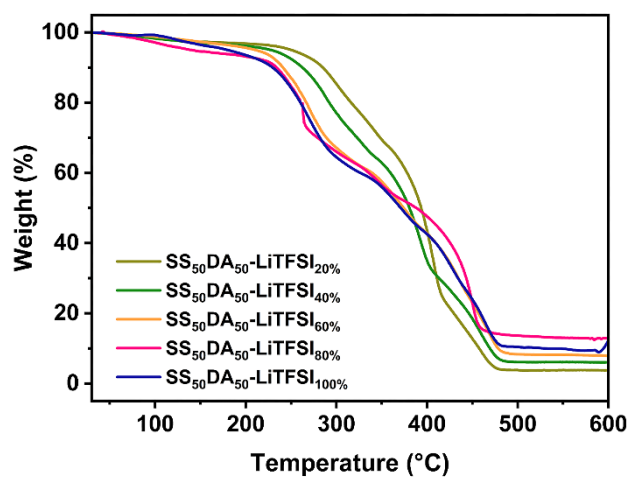
Fig. S21 TGA curves of $SS_{50}DA_{50}$–LiTFSI$_{z\%}$ ionic conductive elastomers at 10 °C·min^{-1} under N$_2$ atmosphere, indicating their excellent thermal stability.
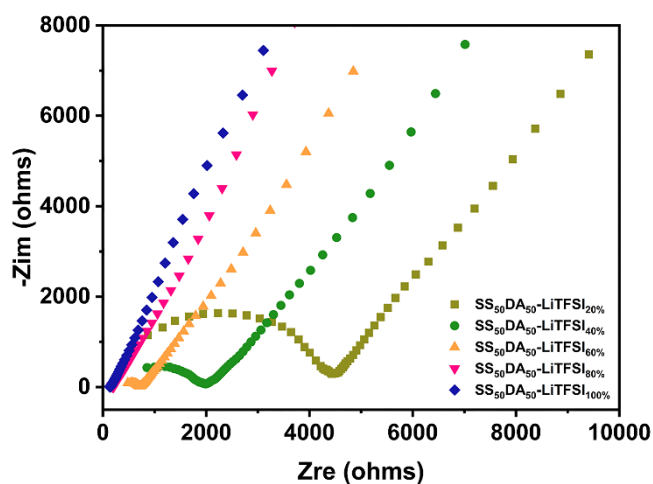
Fig. S22 EIS spectrum of $SS_{50}DA_{50}$–LiTFSI$_{z\%}$ ionic conductive elastomer at room temperature. Test conditions: test voltage of 1 V, frequency range: 10^{-3}–10^6 Hz.
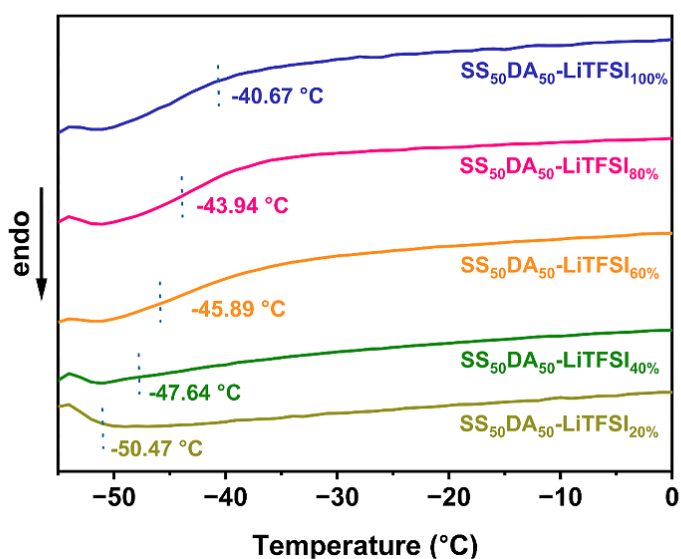
Fig. S23 DSC curves of $SS_{50}DA_{50}$–$LiTFSI_{z\%}$ ionic conductive elastomers. The glass transition temperature (T_g) of $SS_{50}DA_{50}$–$LiTFSI_{z\%}$ increased with the increase of LiTFSI content.
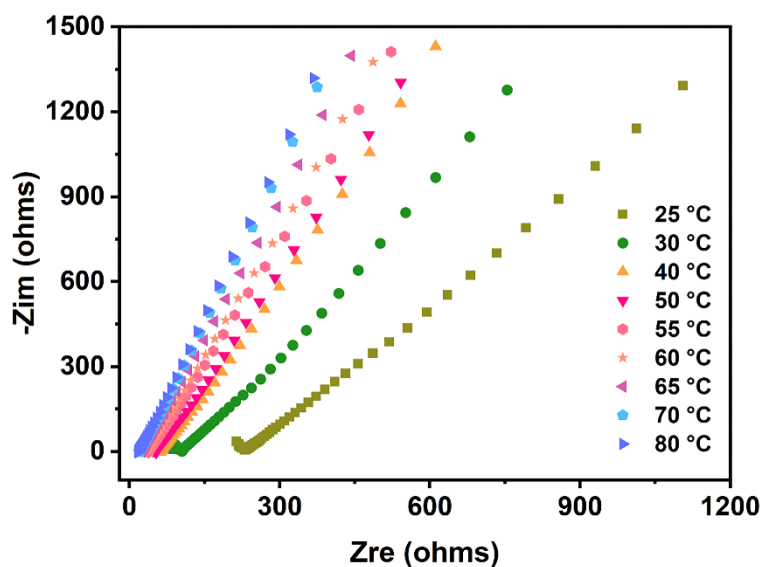
Fig. S24 EIS spectra of $SS_{50}DA_{50}$–$LiTFSI_{80\%}$ samples at different temperatures (25–80°C) with a test voltage of 1 V and a frequency range: 10^{-3}–10^6 Hz.

Table S2. The mechanical properties and ionic conductivity of $SS_{50}DA_{50}$–$LiTFSI_{80\%}$ material compared to previously reported ionic conductive materials.[2-9]

Ionic conductivity elasterms	mechanical strength (MPa)	Ionic conductivity (mS·cm^{-1})	Reference
ICE–0.5$_M$	1.32	1.35×10^{-3}	S2
P(MEA–*co*–IBA)/LiTFSI	1.6	3.76×10^{-3}	S3
THICE	0.5	1.0×10^{-3}	S4
DC–PEO/LiTFSI	0.24	0.204	S5
DICDBNs	0.12	0.205	S6
TEOA0.10–PTA@LiTFSI	0.84	7.35×10^{-2}	S7
ICFE	0.77	3.5×10^{-2}	S8
ICE–C2.0	0.2	8.8×10^{-2}	S9
$SS_{50}DA_{50}$–$LiTFSI_{80\%}$	**1.18**	**0.14**	**This work**
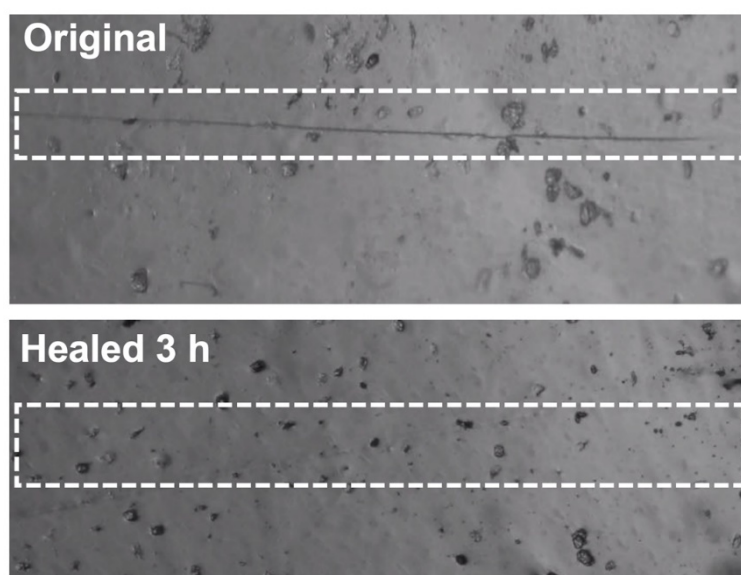
Fig. S25 Optical microscope photographs of $SS_{50}DA_{50}$–$LiTFSI_{80\%}$ samples before and after healing of scratch, healing condition: heating for 3 h at 80 °C.
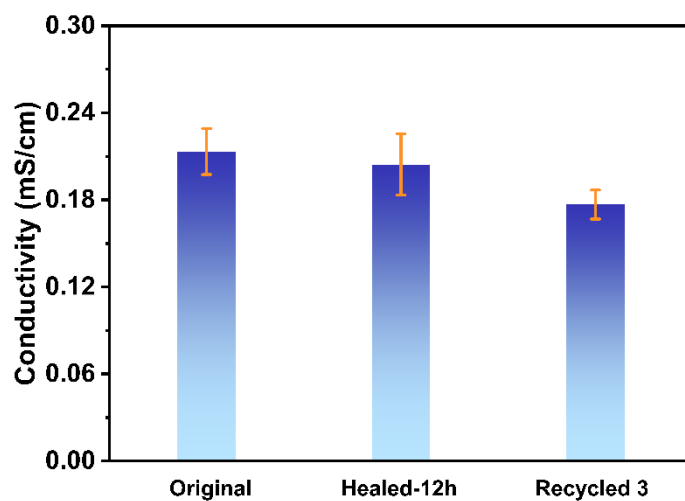
Fig. S26 The ionic conductivity of original, healed, and recycled $SS_{50}DA_{50}$–$LiTFSI_{80\%}$.
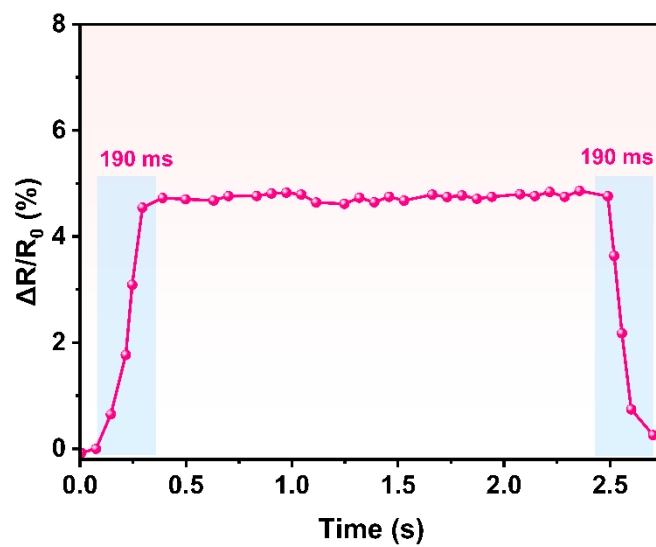
Fig. S27 Response and recovery time curves under 5% strain.
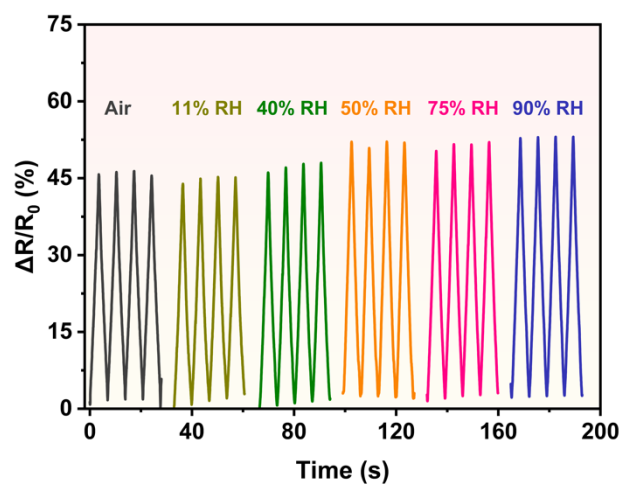
Fig. S28 Relative resistance change of $SS_{50}DA_{50}$-LiTFSI$_{80\%}$ in air and at different humidities (RH 11%, 40%, 50%, 75%, and 90%, respectively), test conditions: strain 50%, tensile rate 60 mm/min.
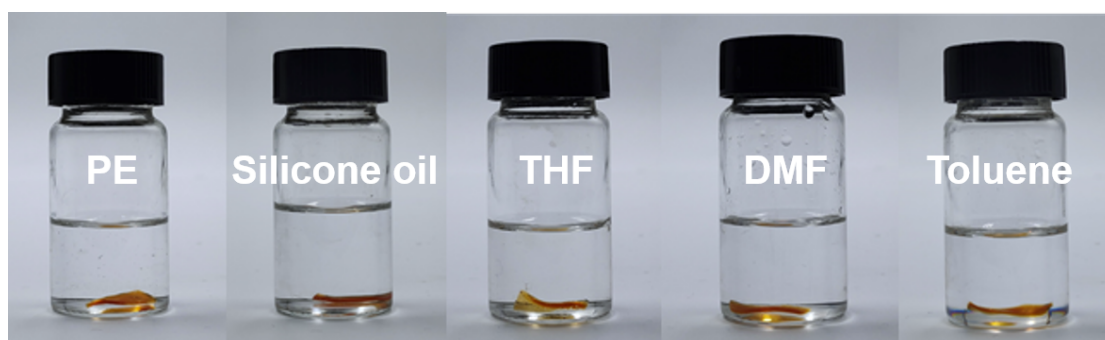
Fig. S29 Photographs of $SS_{50}DA_{50}$-LiTFSI$_{80\%}$ dissolution tests on different organic solvents.

Table S3. The dissolution test data of SS50DA50-LiTFSI80% in different organic solvents.

Solvent	M_0-Before(g)	M_1-After(g)	Swelling ratio(%)
THF	0.135 g	0.843 g	524.0
DMF	0.125 g	0.877 g	602.0
PE	0.151 g	0.171 g	132.0
Toluene	0.134 g	0.177 g	32.1
dimethylsilicon oil	0.145 g	0.152 g	4.8

Swelling ratio (%) = $(M_1-M_0)/M_0 \cdot 100\%$
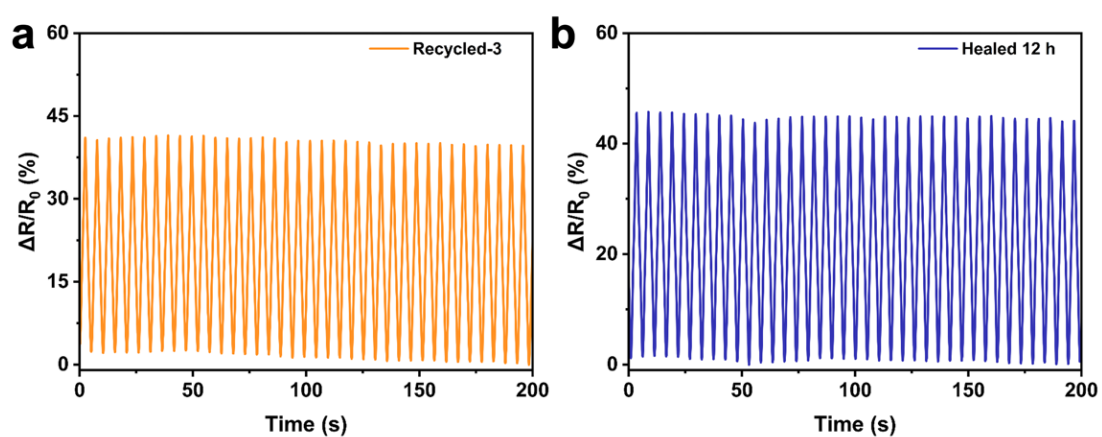
Fig. S30 a) Hot press recycled and b) healing SS$_{50}$DA$_{50}$–LiTFSI$_{80\%}$ films were subjected to a 200 s sensing test at 50% strain. The relative resistance changes of SS$_{50}$DA$_{50}$–LiTFSI$_{80\%}$ are nearly constant, indicating excellent sensing stability.
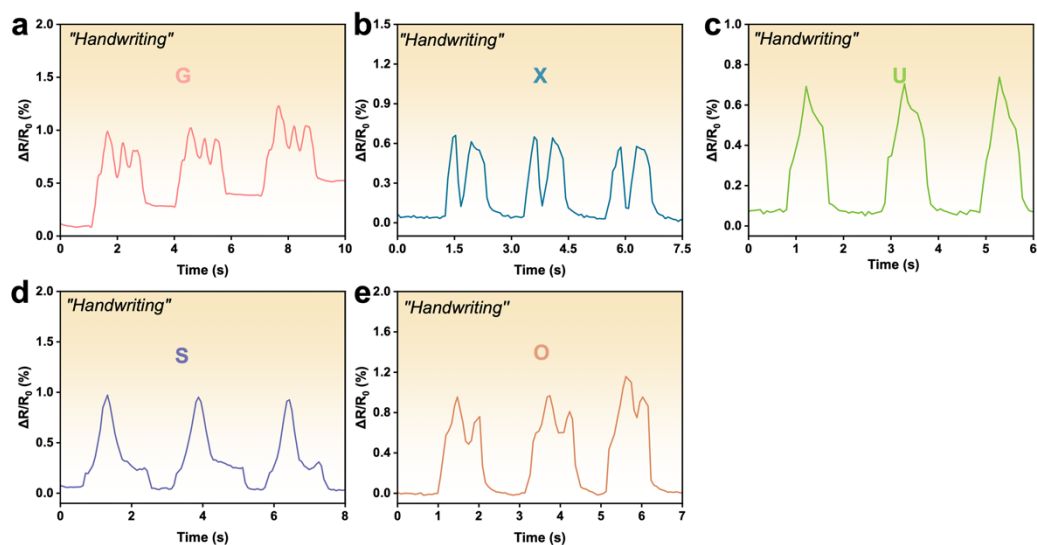
Fig. S31 Based on $SS_{50}DA_{50}$–$LiTFSI_{80\%}$ pressure sensors for recognizing resistance changes when writing letters, relative resistance change rate for writing letters a) "G", b) "X", c) "U", d) "S", e) "O".
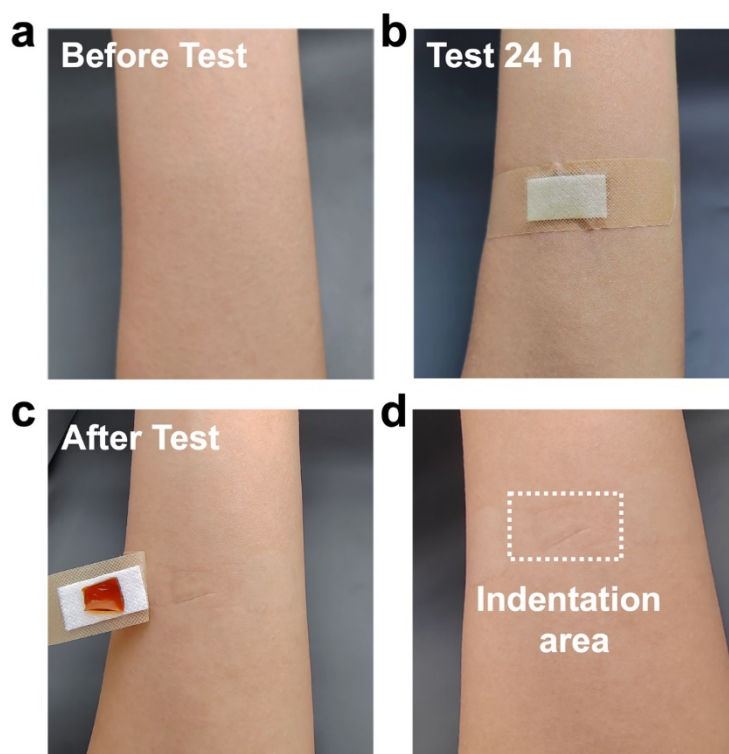
Fig. S32 $SS_{50}DA_{50}$–$LiTFSI_{80\%}$ film with good biocompatibility and no adverse reactions in the volunteer arm.
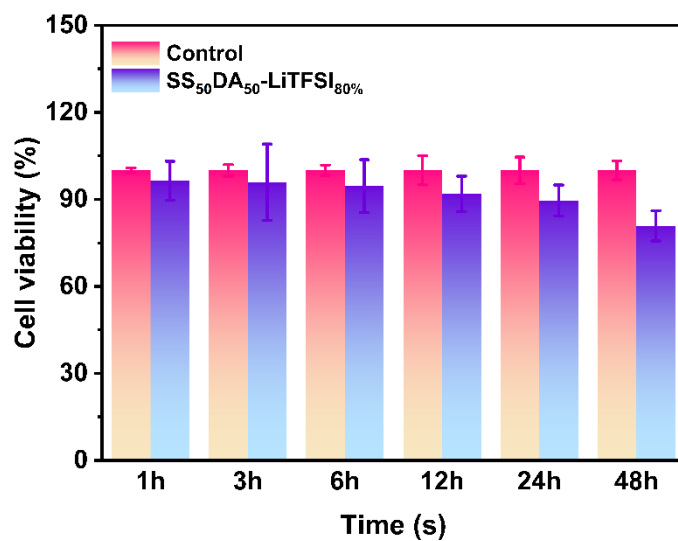
Fig. S33 CCK–8 determination for cell viability of MCF 10A cells cultured in extracts of $SS_{50}DA_{50}$–$LiTFSI_{80\%}$ samples for different times of incubation.
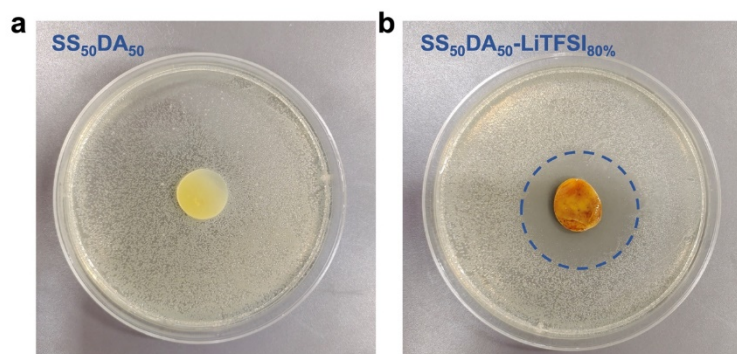
Fig. S34 The inhibition region and diameters of a) $SS_{50}DA_{50}$ and b) $SS_{50}DA_{50}$–$LiTFSI_{80\%}$ film samples against E. coli bacterial, indicating $SS_{50}DA_{50}$–$LiTFSI_{80\%}$ has good antimicrobial properties.
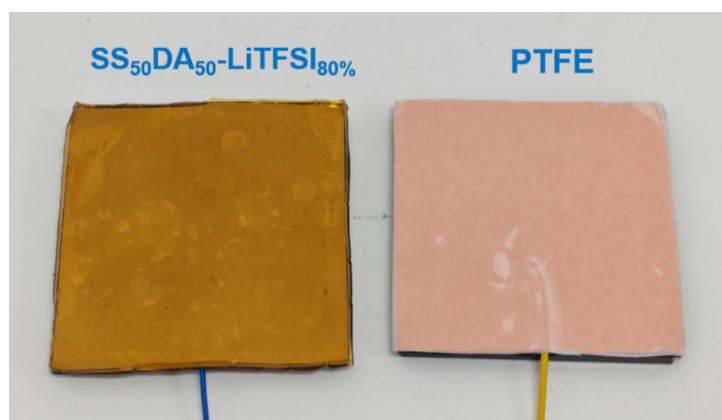
Fig. S35 The digital photo of ICE–TENG.
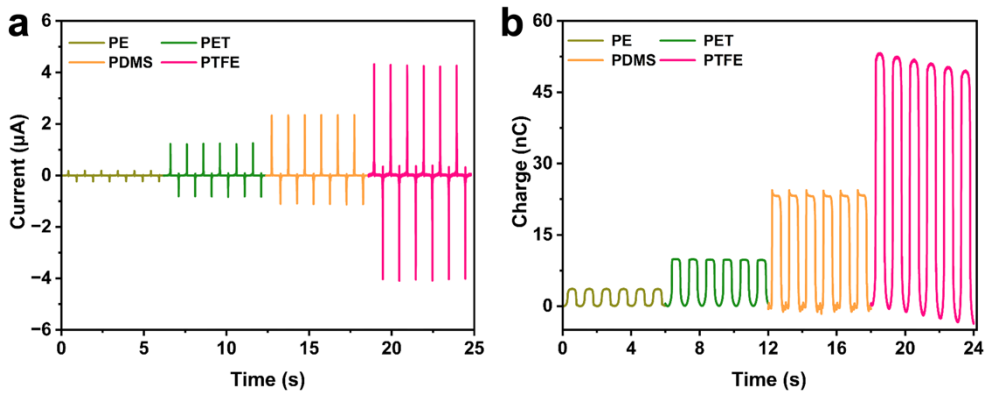
Fig. S36 a) The short–circuit current and b) transferred charge of ICE–TENG prepared with different materials as negative triboelectric layers.
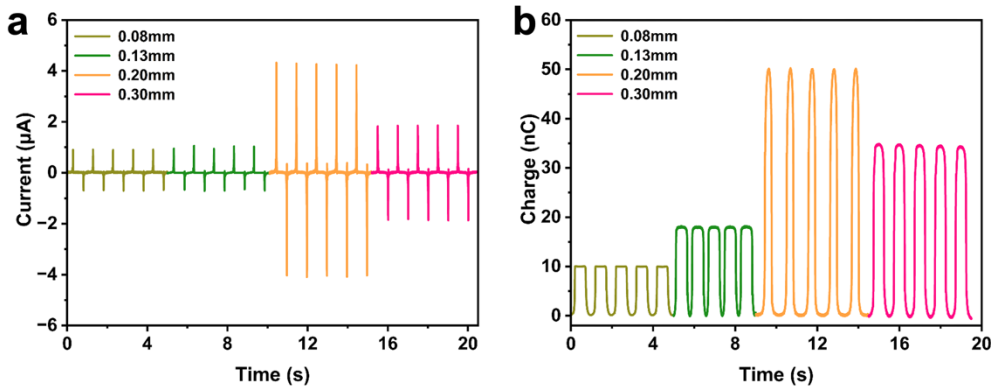
Fig. S37 The short–circuit current a) and transferred charge b) of ICE–TENG prepared with different thicknesses of PTFE films as negative triboelectric layers.
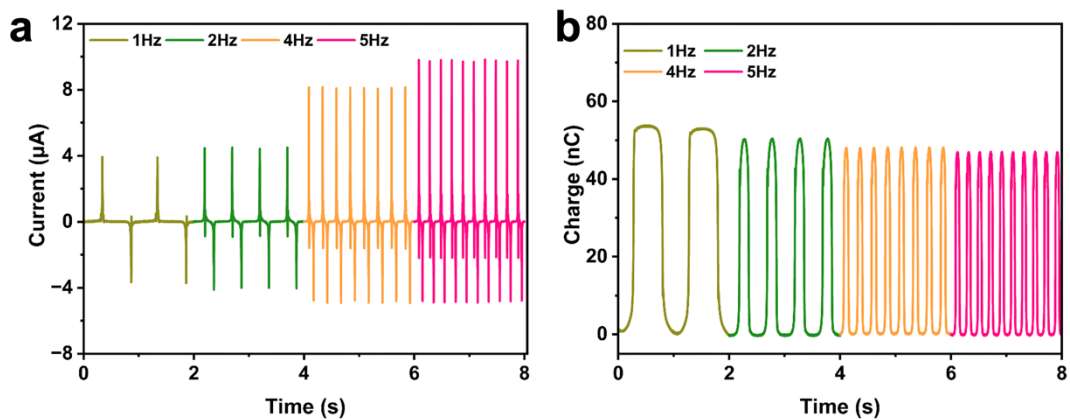
Fig. S38 The short–circuit current a) and transferred charge b) of ICE–TENG at different motion frequencies.
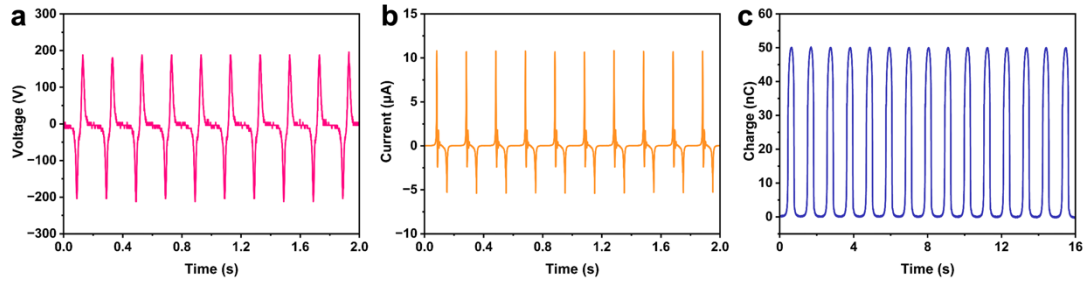
Fig. S39 a) The open–circuit voltage, b) short–circuit current, and c) transferred charge of ICE–TENG at an operating frequency of 5 Hz.
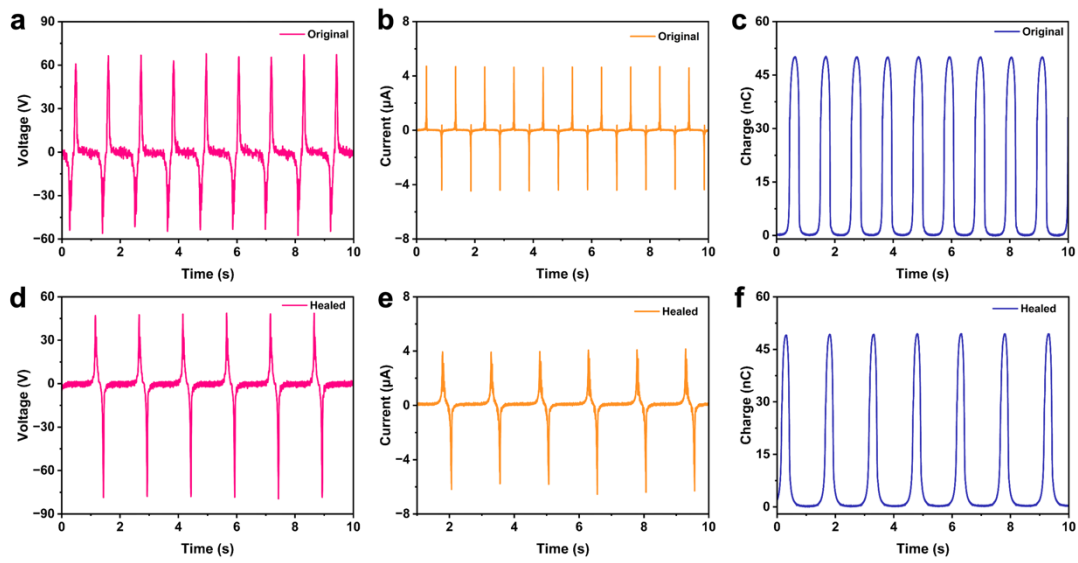
Fig. S40 ICE–TENG output performance before and after healing.

Table S4. Open circuit voltages, short circuit currents, and power densities of ICE–TENG at different loads.

Resistance (Ω)	Voltage (V)	Current (μA)	Power density (W·m⁻²)
1.0×10^3	12	8.17	0.062
1.0×10^4	12	8.17	0.062
1.0×10^5	12	8.17	0.062
2.5×10^6	20	7.96	0.100
5.0×10^6	44	7.77	0.214
7.5×10^6	60	7.44	0.279

1.25×10⁷	92	7.08	0.407
2.5×10⁷	132	6.39	0.527
3.75×10⁷	164	5.92	0.607
5.0×10⁷	188	5.66	0.665
7.5×10⁷	220	5.12	0.703
1.25×10⁸	256	4.50	0.720
2.5×10⁸	292	3.60	0.657
7.5×10⁸	324	289	0.585
1.0×10⁹	324	2.63	0.532
5.0×10⁹	324	1.50	0.304
9.0×10⁹	324	1.20	0.242

Table S5. Comparison of the recently reported overall performance (Open–circuit voltage, Short–circuit current, transferred charge, instantaneous power density, and healing properties) of the ICE–TENG, which has an excellent overall performance.[5, 10-18]

Healing TENG	V_{OC} (V)	Q_{SC} (nC)	I_{SC} (µA)	Power density (mW·m⁻²)	Healing efficiency (%)	Reference
V-PANI-TENG	75	45	6.2	148.5	100	S10
ICE–iTENG	90	30	1.25	55.9	92.2	S11
IU–TENG	95	43	9.5	300	100	S12
DA–TENG	58	17.5	3.2	259	90	S13
OG–TENG	157	29	16	710	98	S14
US–TENG	140	40	1.5	127	100	S15
SH–TENG	100	12	4	400	100	S16
FSASC-TENG	47	17	0.37	2	100	S17
i–TENG	120	40	1.9	127	100	S5

E-TENG	210	60	1	53	95	S18
ICE–TENG	**464**	**16**	**50**	**720**	**100**	**Our work**

3. Supplementary Movies

Movie S1. Using the ICE–TENG to light up 162 LEDs.

Movie S2. Powering a LCD by the ICE–TENG.

4. References

1   S. Ren, H. Liang, P. Sun, Y. Gao and L. Zheng, *New J. Chem.*, 2020, **44**, 1609-1614.

2   C. Luo, Y. Chen, Z. Huang, M. Fu, W. Ou, T. Huang and K. Yue, *Adv. Funct. Mater.*, 2023, **33**, 2304486.

3   B. Yiming, Y. Han, Z. Han, X. Zhang, Y. Li, W. Lian, M. Zhang, J. Yin, T. Sun and Z. Wu, *Adv. Mater.*, 2021, **33**, 2006111.

4   Z. Wu, Y. Guo, M. Qin, C. Liao, X. Wang and L. Zhang, *J. Mater. Chem. A*, 2023, **11**, 16074-16083.

5   P. Zhang, W. Guo, Z. H. Guo, Y. Ma, L. Gao, Z. Cong, X. J. Zhao, L. Qiao, X. Pu and Z. Wang, *Adv. Mater.*, 2021, **33**, 2101396.

6   Y. Tan, H. Chen, W. Kang and X. Wang, *Macromolecules*, 2022, **55**, 9715-9725.

7   K. Zhang, S. Chen, Y. Chen, L. Jia, C. Cheng, S. Dong and J. Hao, *Langmuir*, 2022, **38**, 11994-12004.

8   P. Shi, Y. Wang, K. Wan, C. Zhang and T. Liu, *Adv. Funct. Mater.*, 2022, **32**, 2112293.

9   Z. Chen, F. Li, L. Zhang, Z. Lei, C. Yang, C. Xiao, L. Lian, X. Yuan, G. Ijaz and Z. Lin, *Chem. Eng. J.*, 2023, **451**, 138672.

10   K. Hou, X. Dai, S. Zhao, L. Huang and C. Li, *Nano Energy*, 2023, **116**, 108739.

11   P. Zhang, Y. Chen, Z. H. Guo, W. Guo, X. Pu and Z. Wang, *Adv. Funct. Mater.*, 2020, **30**, 1909252.

12   X. Dai, L. Huang, Y. Du, J. Han, Q. Zheng, J. Kong and J. Hao, *Adv. Funct. Mater.*, 2020, **30**, 1910723.

13   B. Cheng, C. Lu, Q. Li, S. Zhao, C. Bi, W. Wu, C. Huang and H. Zhao, *J. Polym. Environ.*, 2022, **30**, 5252-5262.

14   L. Huang, X. Dai, Z. Sun, M. Wong, S. Pang, J. Han, Q. Zheng, C. Zhao, J. Kong and J. Hao, *Nano Energy*, 2021, **82**, 105724.

15   J. Jiang, Q. Guan, Y. Liu, X. Sun and Z. Wen, *Adv. Funct. Mater.*, 2021, **31**, 2105380.

16   K. Parida, G. Thangavel, G. Cai, X. Zhou, S. Park, J. Xiong and P. S. Lee, *Nat. Commun.*, 2019, **10**, 2158.

17   A. Khan, S. Ginnaram, C. Wu, H. Lu, Y. Pu, J. I. Wu, D. Gupta, Y. Lai and H. Lin, *Nano Energy*, 2021, **90**, 106525.

18   Y. Feng, J. Yu, D. Sun, C. Dang, W. Ren, C. Shao and R. Sun, *Nano Energy*, 2022, **98**, 107284.